

See discussions, stats, and author profiles for this publication at: <https://www.researchgate.net/publication/357382220>

Aerodynamics of a Train and Flat Closed-Box Bridge System with Train Model Mounted on the Upstream Track

Article in *Applied Sciences* · December 2021

DOI: 10.3390/app12010276

CITATIONS

3

READS

135

3 authors, including:



Li Huan

Central South University

34 PUBLICATIONS 271 CITATIONS

[SEE PROFILE](#)



Xuhui He

Central South University

313 PUBLICATIONS 4,322 CITATIONS

[SEE PROFILE](#)

Aerodynamic properties of a streamlined bridge-girder under the interference of trains

Huan Li^{1,2,3}, Xuhui He^{1,2,3}, Liang Hu^{*4} and Xiaojun Wei^{1,2,3}

¹National Engineering research center for High Speed Railway construction, Central South University, Changsha 410075, China

²School of civil engineering, Central South University, Changsha 410075, China

³Hunan Provincial Key Laboratory for Disaster Prevention and Mitigation of Rail Transit Engineering Structure, Changsha, 410075, China

⁴NatHaz Modeling Laboratory, University of Notre Dame, Notre Dame, IN46556, USA

(Received November 15, 2021, Revised April 25, 2022, Accepted August 24, 2022)

Abstract. Trains emerging on a streamlined bridge-girder may have salient interference effects on the aerodynamic properties of the bridge. The present paper aims at investigating these interferences by wind tunnel measurements, covering surface pressure distributions, near wake profiles, and flow visualizations. Experimental results show that the above interferences can be categorized into two primary effects, i.e., an additional angle of attack (AoA) and an enhancement in flow separation. The additional AoA effect is demonstrated by the upward-moved stagnation point of the oncoming flow, the up-shifted global symmetrical axis of flow around the bridge-girder, and the clockwise-deflected orientation of flow approaching the bridge-girder. Due to this additional AoA effect, the two critical AoAs, where flow around the bridge-girder transits from trailing-edge vortex shedding (TEVS) to impinging leading-edge vortices (ILEV) and from ILEV to leading-edge vortex shedding (LEVS) of the bridge-girder are increased by 4° with respect to the same bridge-girder without trains. On the other hand, the underlying flow physics of the enhancement in flow separation is the large-scale vortices shedding from trains instead of TEVS, ILEV, and LEVS governed the upper half bridge-girder without trains in different ranges of AoA. Because of this enhancement, the mean lift and moment force coefficients, all the three fluctuating force coefficients (drag, lift, and moment), and the aerodynamic span-wise correlation of the bridge-girder are more significant than those without trains.

Keywords: aerodynamics; streamlined bridge-girder; wind engineering; wind tunnel test

1. Introduction

Streamlined bridge-girders have been widely used in the China railway high-speed (CRH), such as Bianyuzhou Yangtze River Bridge, Lingang Yangtze River Bridge, and Ganjiang Railway Bridge. Characterized by low stiffness, mass, and damping, bridge-girder with this type is sensitive to crosswinds. Moreover, the aerodynamic properties of these streamlined bridge-girders are also susceptible to shape modifications (Larose and Mann 1998; Païdoussis, Price *et al.* 2010, He, Li *et al.* 2017). Therefore, the presence of trains may have major effects on the wind-resistance performance of these wind-sensitive bridges (Li, Hu *et al.* 2014, Li, Wang *et al.* 2018, Wang, Li *et al.* 2018). For example, a literature review reveals that the presence of trains intensifies the lateral wind-induced response of long-span railway bridges (Li, Qiang *et al.* 2005, Xia, Zhang *et al.* 2006, Xu and Ding 2006, Olmos and Astiz 2018, Olmos and Astiz 2018, Xiang, Tang *et al.* 2020). Moreover, all the wind-induced lateral dynamic loads on the train-bridge system are borne by the bridge-girder. Hence, it is necessary to gain a deep insight into the aerodynamic characteristics of streamlined bridge-girders with trains.

In the past decades, aerodynamic aspects of streamlined

bridge-girders have been thoroughly discussed, covering flow features, aerodynamic forces, wind-induced vibrations, and aerodynamic optimization measures. Typical flow patterns around streamlined bridge-girders include the leading-edge vortex shedding (LEVS), impinging leading-edge vortices (ILEV), trailing-edge vortex shedding (TEVS), and alternate-edge vortex shedding (AVES) (Deniz and Staubli 1997, Païdoussis *et al.* 2010, He, Li *et al.* 2017). In crosswinds, the flow-bridge interactions lead to aerostatic and aeroelastic forces acting on the bridge-girder. For engineering applications, aerodynamic force coefficients, flutter derivatives, and admittance functions are utilized to address the wind-induced forces acting on bridge-girders both in the time domain and frequency domains based on the strip assumption and quasi-steady theory (Larose and Mann 1998, Chen and Kareem 2002, Caracoglia and Jones 2003, Diana *et al.* 2010, Wu and Kareem 2011, Wu and Kareem 2013, Zhu, Meng *et al.* 2013, Mannini *et al.* 2016, Zhou *et al.* 2019). Although with accuracy acceptable in practice, further improvements on modeling and understanding of the wind-induced forces are still needed (Li *et al.* 2018, Zhu *et al.* 2018, Ma *et al.* 2019). As an elongated bluff body, the streamlined bridge-girder is prone to vortex-induced vibration, flutter, and buffeting (Jain *et al.* 1996, Larose and Livesey 1997, Wang *et al.* 2014, Xu *et al.* 2019, Lystad *et al.* 2020, Yang *et al.* 2020, Liao *et al.* 2021, Liu *et al.* 2021). To mitigate this wind-induced vibration, bridge-girder tailoring and additional aerodynamic

*Corresponding author, Professor
E-mail: peettr@gmail.com

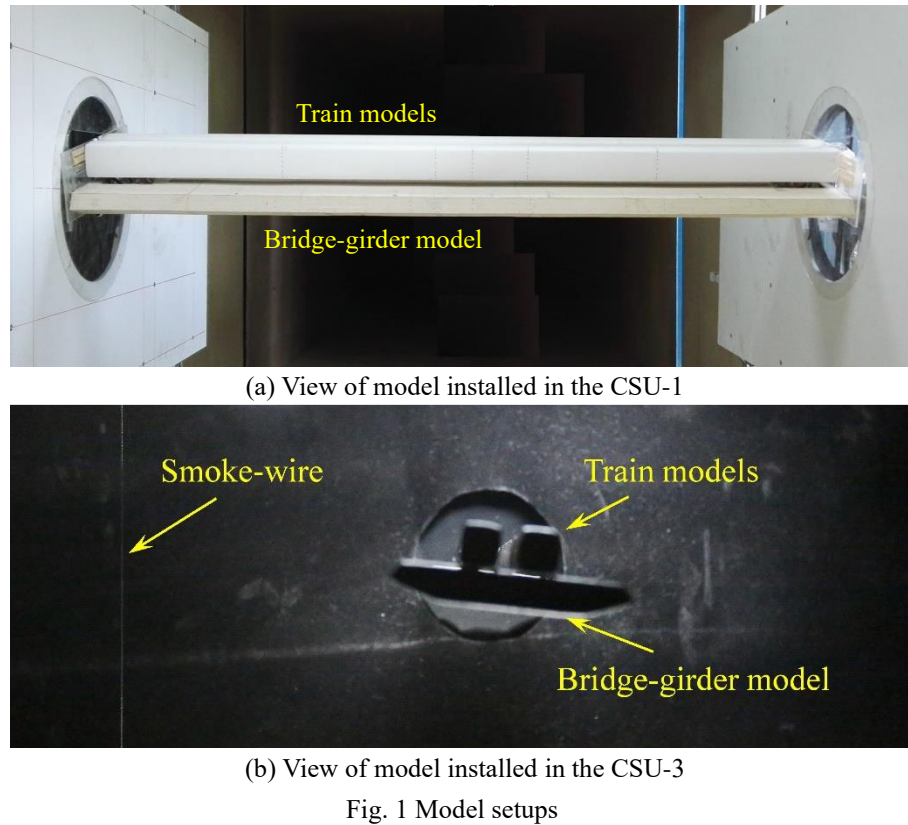


Fig. 1 Model setups

Table 1 Test conditions

| Experiment type | α ($^{\circ}$) | Wind speed (m/s) |
|--|------------------------------|--|
| Surface pressure & wake profile measurements | $-12 - 12, \Delta\alpha = 2$ | 4, 8, 12, 16, and 20 (uniform oncoming flow) |
| Flow visualization | | 4 (uniform oncoming flow) |

optimization measures (guide vanes, spoilers, and so on) have been examined (Larsen and Wall 2012, Montoya *et al.* 2018, Madaniyazi *et al.* 2020). However, studies on the aerodynamic properties of streamlined bridge-girders under the interference of trains are limited.

Currently, there are two kinds of experimental methods to investigate the above-mentioned interference effect, namely static model and moving model tests. The static model test is widely utilized to study the steady and unsteady aerodynamic forces of the train-bridge system and their underlying flow mechanisms (Barcala and Meseguer 2007, Barcala and Meseguer 2008, Guo *et al.* 2014, Ogueta-Gutiérrez *et al.* 2014, Xiang *et al.* 2015, Ma *et al.* 2018), and the results are stable and reliable. But for the moving model test, it usually takes more than a dozen repeated tests to achieve satisfactory results (Baker 2014), and the run-by-run variation could be significant (Baker 2010). Moreover, several technical issues, i.e., unnecessary model vibration, excessive short sampling duration, and the implausible ratio between the train speed and the wind speed of the moving model test have been remaining unsolved. Thus, the present study is carried out on static model test.

Based on the preceding discussion, the present paper aims at revealing the aerodynamic interference effects of two interior-trains on a streamlined bridge-girder by a series of wind tunnel tests. In this study, firstly, the wind tunnel

test setups are detailed. Then, aerodynamic force coefficients, Strouhal numbers, and aerodynamic span-wise correlation of the streamlined bridge-girder model with and without interior-train models are discussed. The wind tunnel test results are validated by comparing to several previous studies. Finally, aerodynamic interference effects and their underlying flow physics are revealed by flow visualizations, surface pressure distributions, wake profiles, and power spectral densities (PSDs) of bridge-girder aerodynamic forces.

2. Wind tunnel setups

Figs. 1(a) and 1(b) depicts two experimental setups for surface pressure and near wake measurements, and flow visualizations carried out in the CSU-1 and CSU-3 wind tunnels, respectively. The CSU-1 wind tunnel is a closed-loop one with a test section measured 3000 mm wide, 3000 mm high, and 15000 mm long, whereas the CSU-3 wind tunnel is also a closed-loop one with the test section measured 800 mm wide, 1200 mm high, and 1500 mm long. The incoming flow velocity ranges of the two wind tunnels are 0 ~ 92 m/s with turbulent intensity lower than 0.5% and 0 ~ 25 m/s with turbulent intensity lower than 0.5%, respectively.

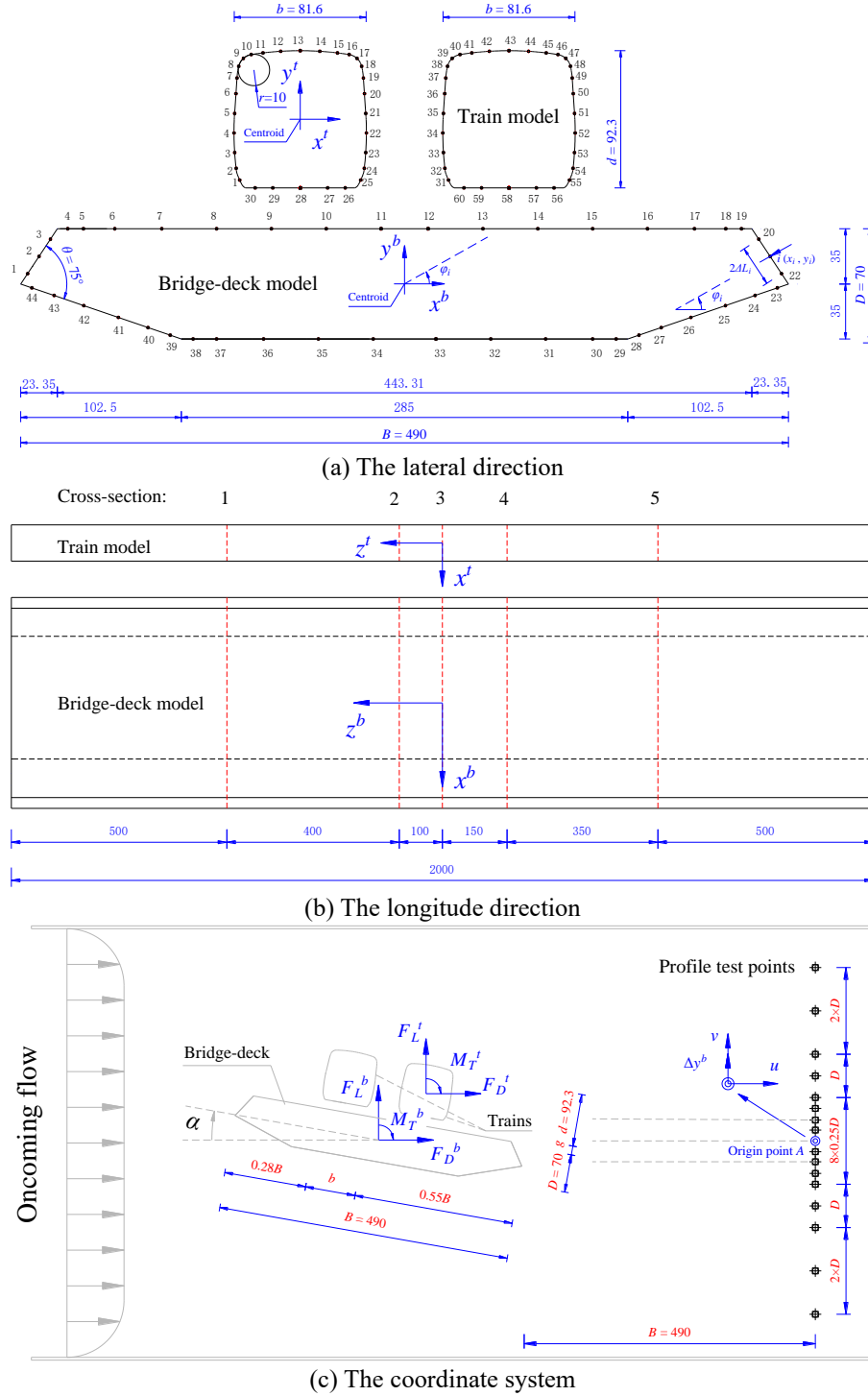


Fig. 2 Geometries of the model installed in the CSU-1. (Unit: mm)

As depicted in Fig. 2, the test model is a generic streamlined bridge-girder simplified from a long-span railway bridge in practice. Bridge-girder attachments (handrails, maintenance rails, track ballast, barriers, and so on) were neglected to highlight the aerodynamic interference effects. According to the cross-sectional dimensions of wind tunnels, two streamlined bridge-girder models with the same scale ratio of 1:40 were designed, respectively. Fig. 2 presents the geometric parameters of the bridge-girder model. The two interior-train models were

also scaled down by 1:40 to match the above bridge-girder model. Fig. 2(c) shows the configurations of the interior-train and bridge-girder models specified by $0.28B$ and $g = 0.14d$, where B and d are the width of the bridge-girder model and the height of the interior-train model, respectively. The model system tested in the CSU-1 was utilized to measure the surface pressure and wake profile, whereas the model system tested in the CSU-3 was used to visualize the flow structures around the model. The coordinate systems x^b - y^b and x^t - y^t located at the geometric

centroids of the bridge-girder and train models are also depicted in Fig. 2, respectively.

The surface of the bridge-girder and train model was pre-installed with $44 \times 5 = 220$ and $60 \times 5 = 300$ pressure taps as presented in Figs. 2(a) and (b), respectively. The surface pressure around the bridge-girder model was recorded by four ZOC33/64Px2 pressure scanners with the sampling frequency of 625 Hz/channel. The sampling duration of each pressure channel was modulated as 32 s. In order to mitigate pressure signal distortion, 520 PVC tubes with the same length of 500 mm were utilized to connect the above pressure taps and pressure scanner channels based on the study of Li, He *et al.* (2019). The mean wind velocity (U_∞) of incoming flow was monitored by a Pitot tube fixed 5000 mm upstream from the nose of the bridge-girder model in the midspan of the CSU-1 wind tunnel.

To measure the wake profiles of the streamlined bridge-girder model, 17 flow test points located at $x = 1.5B$ and $y = [-4D, 4D]$ were utilized as in Fig. 2(c), where D is the height of the bridge-girder model. For the sake of clarity, the above detailed coordinate positions were normalized by D . The normalized Δy_i^b denotes the perpendicular distance between the i^{th} test point and the nose-tail line of bridge-girder model at wind angle of attack (AoA) $\alpha = 0^\circ$. The flow velocities at the 17 test points were measured one-by-one by a Cobra probe (TFI, Series 300) with the sampling frequency of 2 kHz. The sampling duration at each test point was 30 s.

With reference to previous studies (Sarwar *et al.* 2008, He *et al.* 2017, Jiang *et al.* 2021), the aerodynamic properties of the present model were tested in the range of $\alpha = [-12^\circ, 12^\circ]$. In the CSU-1 and CSU-3 wind tunnels, the velocities of free incoming flow were $U_\infty = 20$ m/s and 4 m/s, respectively. The corresponding inflow Reynold numbers (Re) are 2.19×10^5 and 4.38×10^4 based on the train-bridge system height $d + D$ at $\alpha = 0^\circ$, respectively. For the surface pressure & wake profile measurements, the $Re = 2.19 \times 10^5$ meets the recommended value range 2.0 to 2.5×10^5 of the railway vehicle specification for static wind tunnel tests (CEN 2018). Moreover, when the Re is larger than 2×10^5 , the Reynolds number effect on the aerodynamics of the train-bridge system is limited (Suzuki *et al.* 2003, Bocciolone *et al.* 2008, Cheli *et al.* 2010, Xiang *et al.* 2015). Thus, the present aerodynamic test results may be acceptable for full scale application. For flow visualization tests, the $Re = 4.38 \times 10^4$ is much smaller than the above recommended value. However, the present visualization results are chiefly utilized to qualitatively identify the dominated flow patterns around the bridge girder. The Reynolds number may influence the flow transition around the round corners of the train-bridge system but have limited effect on the dominated flow patterns of the whole system as evidenced by Barcala and Meseguer (2008). To further confirm the above-mentioned Reynolds number independent behavior, the surface pressure measurements were also carried out at $U_\infty = 4, 8, 12$, and 16 m/s at $\alpha = 0^\circ$ in the following section, corresponding to inflow $Re = 4.38 \times 10^4, 8.77 \times 10^4, 1.32 \times 10^5$, and 1.75×10^5 , respectively. Table 1 summarizes the test conditions of this study.

3. Results

This section describes the aerodynamic properties of the present streamlined bridge-girder with and without two interior-train models. The tested results are represented as time-averaged aerodynamic forces, Strouhal numbers, and span-wise correlation coefficients for different AoA ranges. For a railway bridge in its design stage, both the aerodynamic properties of the bridge and the dynamic characteristics of the wind-train-bridge system should be fully considered. From this point of view, the time-averaged aerodynamic force coefficients of the two interior-train models are also shown here for further dynamic analyses of the wind-train-bridge system. Compared to experimental results of several previous studies, the present testing is validated.

3.1 Aerodynamic force coefficients

The drag, lift, and moment force coefficients C_D^b , C_L^b , C_M^b , C_D^t , C_L^t , and C_M^t of the bridge-girder and train models in wind axis are expressed as follows, respectively.

$$C_D^b = \left(\sum_{i=1}^N C_{p_i}^b \times \Delta L_i \times \cos \varphi_i \times \cos \alpha + \sum_{i=1}^N C_{p_i}^b \times \Delta L_i \times \sin \varphi_i \times \sin \alpha \right) / B \quad (1)$$

$$C_L^b = \left(-\sum_{i=1}^N C_{p_i}^b \times \Delta L_i \times \cos \varphi_i \times \sin \alpha + \sum_{i=1}^N C_{p_i}^b \times \Delta L_i \times \sin \varphi_i \times \cos \alpha \right) / B \quad (2)$$

$$C_M^b = \left(\sum_{i=1}^N C_{p_i}^b \times \Delta L_i \times \cos \varphi_i \times y_i - \sum_{i=1}^N C_{p_i}^b \times \Delta L_i \times \sin \varphi_i \times x_i \right) / B^2 \quad (3)$$

$$C_D^t = \left(\sum_{i=1}^N C_{p_i}^t \times \Delta L_i \times \cos \varphi_i \times \cos \alpha + \sum_{i=1}^N C_{p_i}^t \times \Delta L_i \times \sin \varphi_i \times \sin \alpha \right) / b \quad (4)$$

$$C_L^t = \left(-\sum_{i=1}^N C_{p_i}^t \times \Delta L_i \times \cos \varphi_i \times \sin \alpha + \sum_{i=1}^N C_{p_i}^t \times \Delta L_i \times \sin \varphi_i \times \cos \alpha \right) / b \quad (5)$$

$$C_M^t = \left(\sum_{i=1}^N C_{p_i}^t \times \Delta L_i \times \cos \varphi_i \times y_i - \sum_{i=1}^N C_{p_i}^t \times \Delta L_i \times \sin \varphi_i \times x_i \right) / b^2 \quad (6)$$

where $C_{p_i}^b = (P_i^b - P_\infty) / 0.5\rho U_\infty^2$ and $C_{p_i}^t = (P_i^t - P_\infty) / 0.5\rho U_\infty^2$, P_i^b and P_i^t are the pressure measured on the i^{th} pressure tap of the bridge-girder and train models, respectively. P_∞ and $0.5\rho U_\infty^2$ are the static and dynamic pressures of the incoming flow tested by the Pitot tube fixed in the free incoming flow, respectively. The geometric parameters α , φ_i , ΔL_i , x_i , and y_i are defined in Fig. 2. \bar{C}_D^b , \bar{C}_L^b , \bar{C}_M^b , \bar{C}_D^t , \bar{C}_L^t , \bar{C}_M^t , $C_D^{b'}$, $C_L^{b'}$, $C_M^{b'}$, $C_D^{t'}$, $C_L^{t'}$, and $C_M^{t'}$ are the mean and standard deviation of C_D^b , C_L^b , C_M^b , C_D^t , C_L^t , and C_M^t , respectively.

The effect of Reynolds number on the aerodynamic force coefficients of the present bridge-girder is examined in $Re = [4.38 \times 10^4, 2.19 \times 10^5]$. As shown in Fig. 3, the mean and fluctuating force coefficients of the bridge-girder

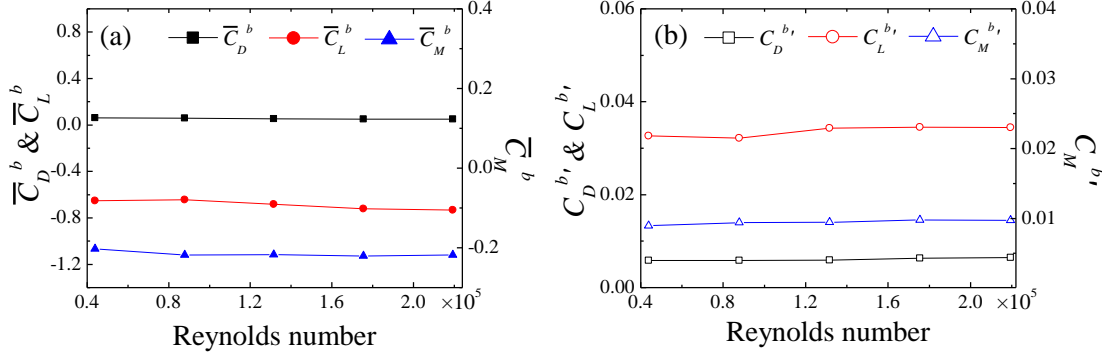


Fig. 3 Aerodynamic force coefficients of the bridge-girder model with double interior-trains in $Re = [4.38 \times 10^4, 2.19 \times 10^5]$ at $\alpha = 0^\circ$. (a) Mean force coefficients, (b) Fluctuating force coefficients

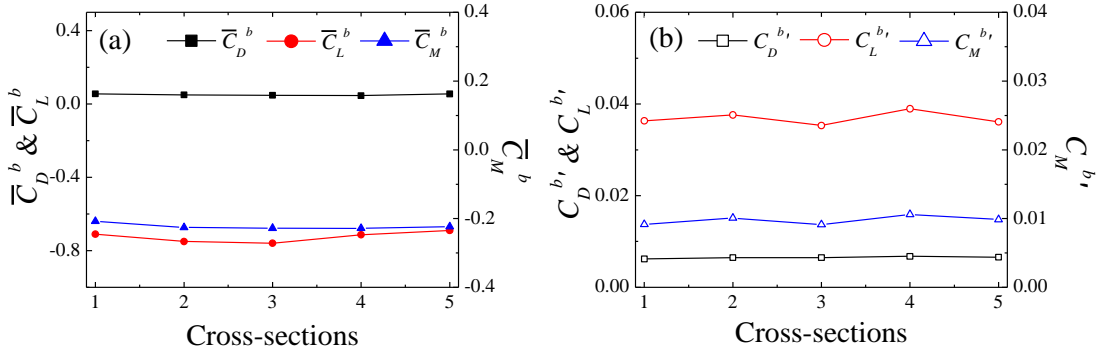


Fig. 4 Aerodynamic force coefficients of the bridge-girder model with double interior-trains along spanwise direction at $\alpha = 0^\circ$. (a) Mean force coefficients, (b) Fluctuating force coefficients

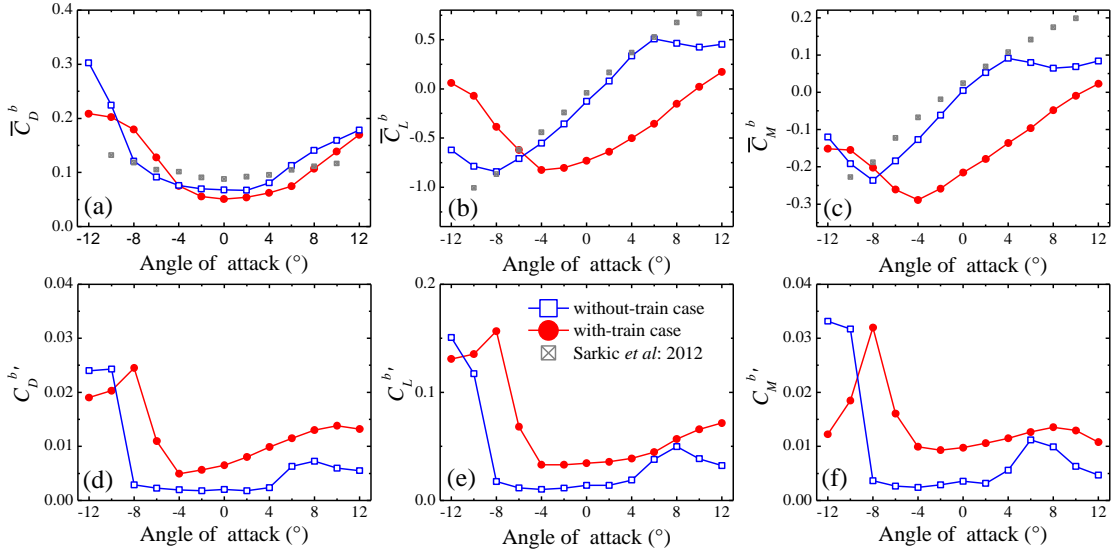


Fig. 5 Aerodynamic force coefficients of the streamlined bridge girder model. (a) - (c) Mean force coefficients, (d) - (f) Fluctuating force coefficients

are almost Re -independent, indicating that the aerodynamic characteristics of the girder model are insensitive to the Reynolds number effect in this Re region. Based on previous studies and this Reynolds number dependency analysis, the Re choices for smoke-wire visualization and surface pressure & wake profile measurements, as demonstrated in section 2, are acceptable.

For the bridge-girder model with interior-trains, the test

results on five pressure-testing-cross-sections along the span-wise direction (Fig. 2(b)) at $\alpha = 0^\circ$ are depicted in Fig. 4. Not surprisingly, the aerodynamic force coefficients of different span-wise locations are almost the same. This uniformity is also observed for all the other AoAs. Therefore, the aerodynamic properties tested at the midspan of the bridge-girder and train models (Fig. 2(b)) are mainly discussed in the remained study.

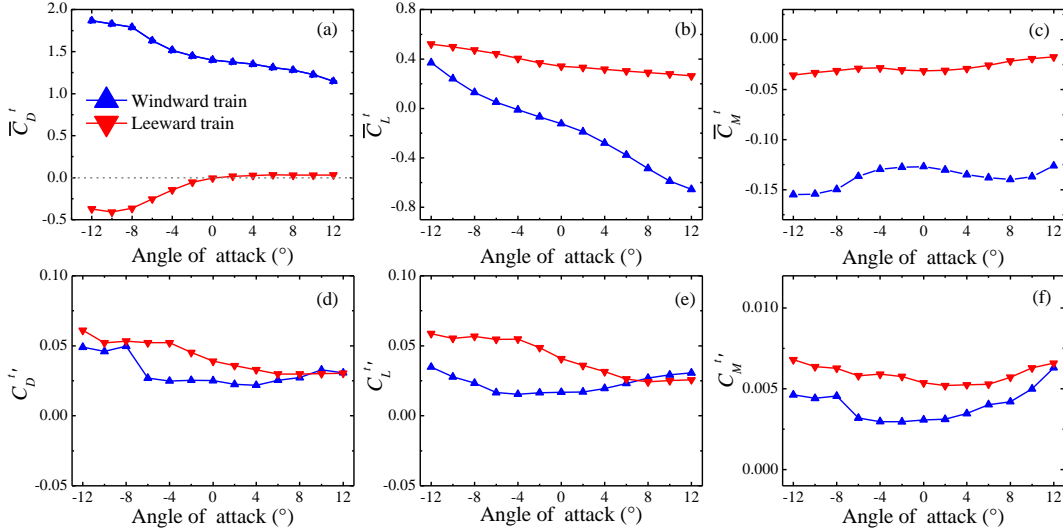


Fig. 6 Aerodynamic force coefficients of the train models. (a) - (c) Mean force coefficients, (d) - (f) Fluctuating force coefficients

Fig. 5 illustrates the aerodynamic force coefficients of the bridge-girder model with and without two interior-train models (with-train and without-train cases for short in the remained discussion) in the range of $\alpha = [-12^\circ, 12^\circ]$. For validation, the wind tunnel testing results of a similar streamlined bridge-girder from Šarkić, Fisch *et al.* (2012) are also included in Fig. 5. Generally, the two wind tunnel tests match well within the allowed experimental error range, verifying the present test in the CSU-1 wind tunnel.

For the with-train case, \bar{C}_D^b minimizes at $\alpha = 0^\circ$ with the value of 0.068, as shown in Fig. 5(a). When α varies beyond 0° but still within $[-4^\circ, 6^\circ]$, \bar{C}_D^b increases at a low rate. With a further increase in $|\alpha|$, \bar{C}_D^b exhibits a linear increase until $\alpha = -8^\circ$ and 12° in the negative and positive regions of α , respectively. In the range of $\alpha = [-12^\circ, -8^\circ]$, the increase of \bar{C}_D^b saturates. The most significant behaviours of both \bar{C}_L^b and \bar{C}_M^b are that they reach their minima at $\alpha = -4^\circ$, where the bridge-girder model is stalled because $|\bar{C}_L^b|$ and $|\bar{C}_M^b|$ decrease abruptly as shown in Figs. 5(b) and 5(c). In He, Li *et al.* (2017) and Guissart, Andrianne *et al.* (2019), the stall of an elongated bluff body is attributed to the flow transition near the reattachment point. Similar to the stall of airfoils, this stall is unfavourable to the aerodynamic stability of streamlined bridge-girders. As α departs from -4° , \bar{C}_L^b and \bar{C}_M^b increase monotonically and both saturate at $\alpha = -10^\circ$. For the fluctuating force coefficients $C_D^{b'}$, $C_L^{b'}$, and $C_M^{b'}$, a sensible plunge at $\alpha = -4^\circ$ divides the range of $\alpha = [-12^\circ, 12^\circ]$ into two parts: noticeable larger fluctuation in force coefficients in $[-12^\circ, -6^\circ]$ is observed than in $[-4^\circ, 12^\circ]$.

Compared to the bridge-girder model without interior-train models depicted in Fig. 5, the interference effects of the two interior-train models on the aerodynamic force coefficients of the streamlined bridge-girder can be mainly identified in three aspects. Firstly, the stall angle of the

streamlined bridge-girder model in the with-train case is 4° smaller than that of the without-train case. Secondly, no stall angle can be observed in the range of $\alpha = [0^\circ, 12^\circ]$ in the with-train case. Finally, the amplitude of $C_D^{b'}$, $C_L^{b'}$, and $C_M^{b'}$ of the bridge-girder in the with-train case is enhanced in the range of $\alpha = [-4^\circ, 12^\circ]$ with respect to the without-train case.

Fig. 6 depicts the aerodynamic force coefficients of the two interior-train models. For the windward train model, \bar{C}_D^t and \bar{C}_L^t decrease monotonously with an increase in $\alpha = [-12^\circ, 12^\circ]$, whereas \bar{C}_M^t increases nonlinearly with a decrease in $|\alpha| = [12^\circ, 0^\circ]$ and saturates at $\alpha = 0^\circ$. Similar to the fluctuating force coefficients of the bridge-girder (Figs. 5(d)-5(f)), a sensible plunge can be observed in the $C_D^{t'}$, $C_L^{t'}$, and $C_M^{t'}$ of the windward train model, but the corresponding α decreases from -4° for the bridge-girder model to -6° for the windward train model, as shown in Figs. 6(d) - 6(f). For the leeward train model, \bar{C}_D^t increases from -0.37 to 0.30 with an increase in $\alpha = [-12^\circ, 6^\circ]$ and then remains almost constant in $\alpha = [6^\circ, 12^\circ]$ as highlighted by a dash line in Fig. 6(a), while \bar{C}_L^t , $C_D^{t'}$, $C_L^{t'}$, and $C_M^{t'}$ reduce gradually in all the test range of α .

By comparison, two primary aerodynamic interference effects between the windward and leeward train models can be identified in Fig. 5. Firstly, the windward train model may have an obvious shielding effect on the leeward one, which results in a negative \bar{C}_D^t and a significant reduced \bar{C}_L^t for the leeward train model in $\alpha = [-12^\circ, 0^\circ]$ and $[0^\circ, 12^\circ]$, respectively. Secondly, the high turbulent near wake of the windward train model noticeably intensify the $C_D^{t'}$, $C_L^{t'}$, and $C_M^{t'}$ of the leeward train model in $\alpha = [-12^\circ, 12^\circ]$. Moreover, the above two effects decay generally with

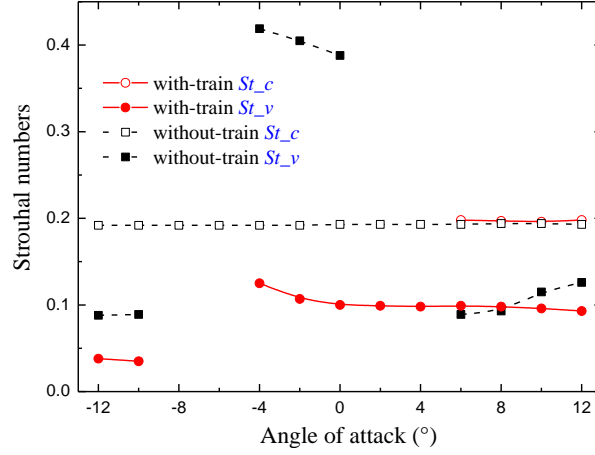


Fig. 7 Strouhal numbers of the streamlined bridge girder model

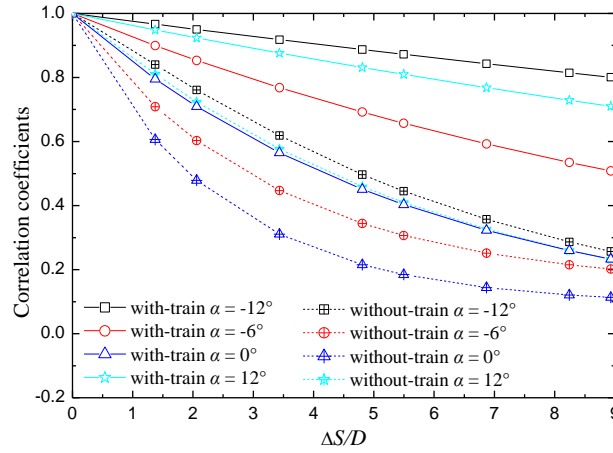


Fig. 8 Spanwise correlation coefficients of the lift force of the streamlined bridge-girder model

an increase in α . Generally speaking, the aerodynamic interference effects between the two interior-train models are quite complicated. Due to the purpose and limitation of the present study, further studies are eagerly required to reveal the detailed information and other influencing factors on the above aerodynamic interference.

3.2 Strouhal number

The Strouhal number ($St = fD/U_\infty$, where f is the dominated frequency of the lift power spectral density of the streamlined bridge-girder) is depicted in Fig. 7. For the without-train case, there are two kinds of Strouhal numbers for the bridge-girder model. Following the study of He *et al.* (2017), the Strouhal numbers dependent on and independent of AoA are denoted as St_v ($St_v = f_v D/U_\infty$, where f_v is the dominated frequency of the TEVS) and St_c ($St_c = f_c D/U_\infty$, where f_c is the dominated frequency of the LEVS), respectively. This double-St-phenomenon is fairly consistent with the studies of Okajima (1982), Parker and Welsh (1983) and Tan, Thompson *et al.* (2003) on rectangular cylinders, and by Larsen and Wall (2012) on streamlined bridge-girders.

For the with-train case, the double-St-phenomenon can

still be detected as shown in Fig. 7. St_c can only be identified in the range of $\alpha = [6^\circ, 12^\circ]$ owing to the presence of two interior-train models. On the other hand, St_v displays three different behaviors in the range of $\alpha = [-12^\circ, 12^\circ]$. In $\alpha = [-4^\circ, 12^\circ]$, St_v decreases generally from 0.125 to 0.093. In $\alpha = [-8^\circ, -6^\circ]$, no St_v can be detected. The underlying flow physics of this St_v disappearance will be revealed by flow visualization and surface pressure in sections 4.1 and 4.2. Finally, St_v remains almost constant in the range of $\alpha = [-12^\circ, -10^\circ]$. Upon comparing to the without-train case, a smaller St_v can be observed in the ranges of $\alpha = [-12^\circ, -10^\circ]$ & $[-4^\circ, 12^\circ]$. However, the value of St_c is not influenced by the two interior-train models.

3.2 Span-wise correlation

Following the study of Ito, Shirato *et al.* (2014), the span-wise correlation coefficient $R(\Delta S)$ of lift force is expressed by Eq. (7), where t denotes the time; $f(t)$ denotes the time history of lift coefficient measured on one of the pressure-testing-cross-sections as shown in Fig. 2(b) and ΔS denotes the distance between two pressure-testing-cross-

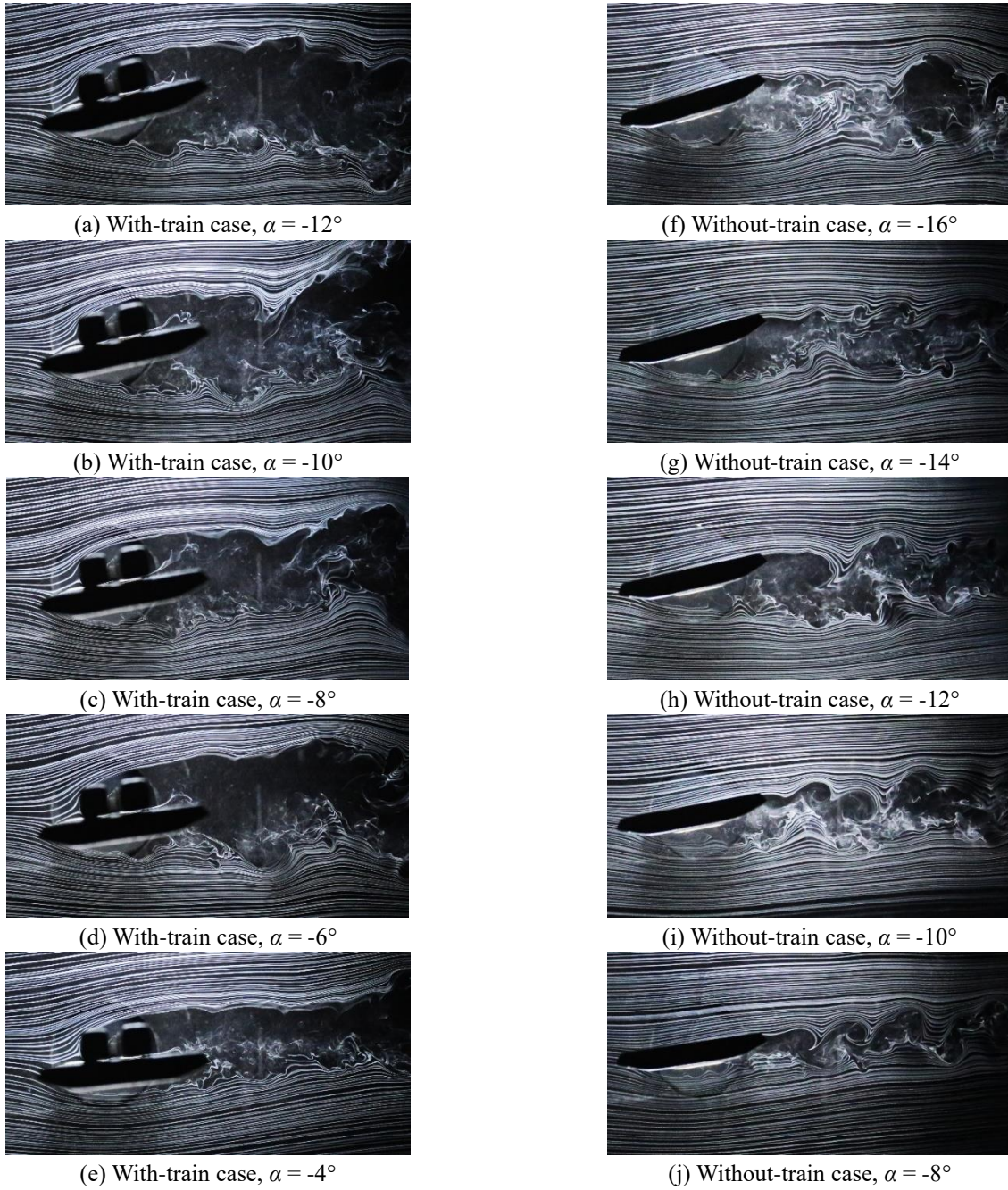


Fig. 9 Instantaneous flow structures around the streamlined bridge girder model. (a) - (e) with-train case $\alpha = -12^\circ \sim -4^\circ$, (f) - (j) without-train case $\alpha = -16^\circ \sim -8^\circ$

sections along the spanwise direction. The $R(\Delta S)$ s of lift coefficient in both the with-train and without-train cases are shown in Fig. 8. Based on the behaviors of aerodynamic force coefficients and Strouhal numbers discussed above, only the results at four selected $\alpha = -12^\circ, -6^\circ, 0^\circ$, and 12° are presented here for brevity.

$$R(\Delta S) = \frac{\overline{f(t,0)f(t,\Delta S)}}{\sqrt{f(t,0)^2} \sqrt{f(t,\Delta S)^2}} \quad (7)$$

Generally, all the eight curves of the correlation coefficients in Fig. 8 decay with the increase in the normalized span-wise distance $\Delta S/D$ but at different

decrease rates. A larger correlation coefficient can be detected in the with-train case than the without one, suggesting the span-wise correlation of the aerodynamic properties of the bridge-girder model is stronger with presence of the two interior-train models.

4. Discussions

In this section, the underlying flow physics of the aerodynamic interference effects of two interior-train models on the aerodynamic properties of the streamlined bridge-girder model are revealed by a joint analysis of flow

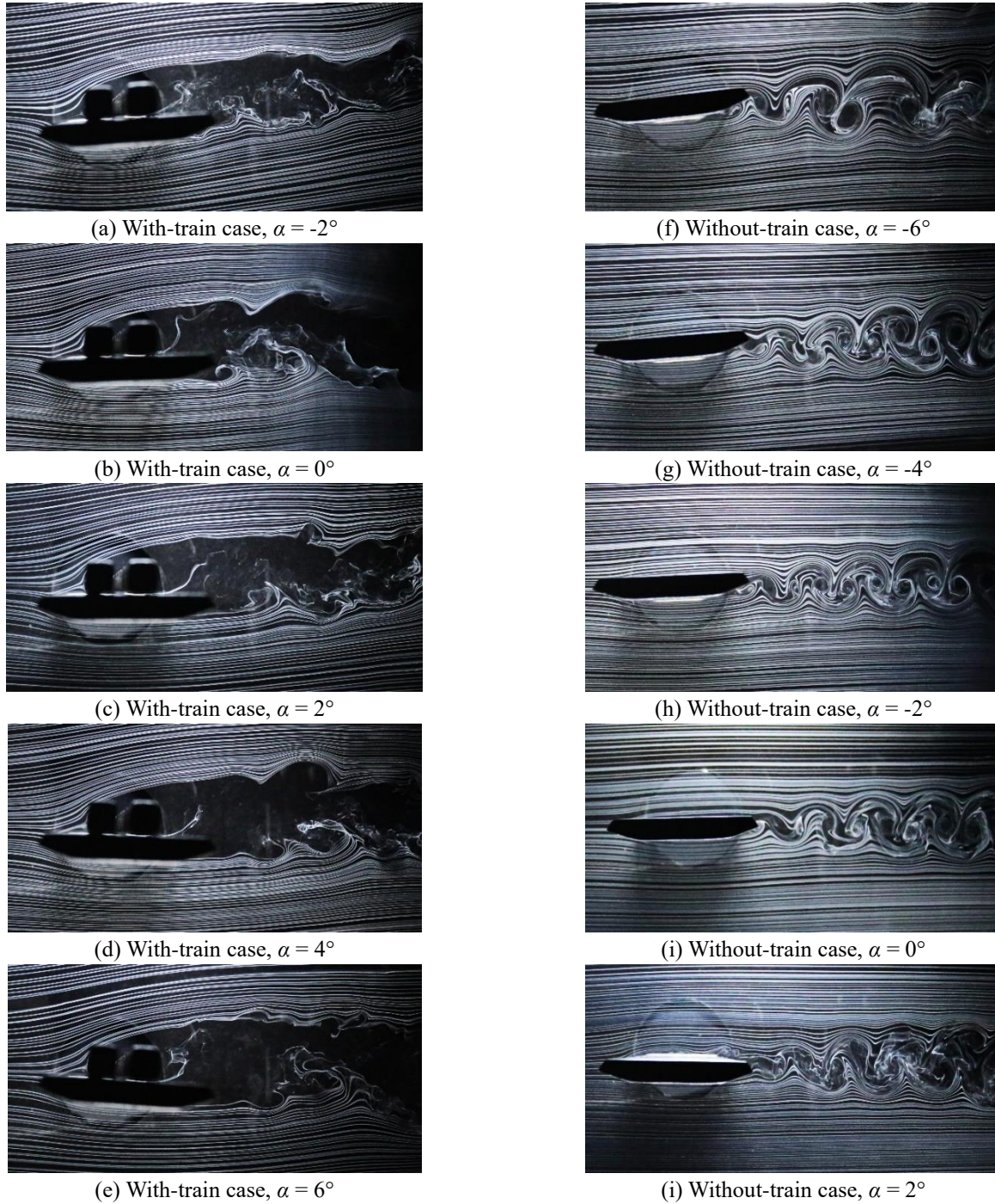


Fig. 10 Instantaneous flow structures around the streamlined bridge girder model. (a) - (e) with-train case $\alpha = -2^\circ \sim 6^\circ$, (f) - (j) without-train case $\alpha = -6^\circ \sim 2^\circ$

visualization results, surface pressure measurements, wake profiles, and the PSDs of lift force. With these flow physics, the aerodynamic properties discussed in the preceding sections are explained.

4.1 Flow visualizations

Smoke-wire visualization is widely utilized to acquire flow structures around bluff bodies (Huang *et al.* 2010, Païdoussis *et al.* 2010, Yen and Yang 2011). For elongated bluff bodies in incident flow, three typical flow patterns,

i.e., TEVS, ILEV, and AVES, have already been identified by many previous studies as reviewed in the introduction of the present paper.

Figs. 9-11 demonstrate the ‘instantaneous’ flow structures around the present models captured in the CSU-3 wind tunnel. For the with-train case, as depicted in left columns, the predominated characteristics of flow structures around the streamlined bridge-girder can be classified into three regions with an increase in α , i.e., $\alpha = [-12^\circ, -10^\circ]$, $\alpha = [-8^\circ, -6^\circ]$, and $\alpha = [-4^\circ, 12^\circ]$. In $\alpha = [-12^\circ, -10^\circ]$, the upper half of the bridge-girder is governed by large-scale vortex

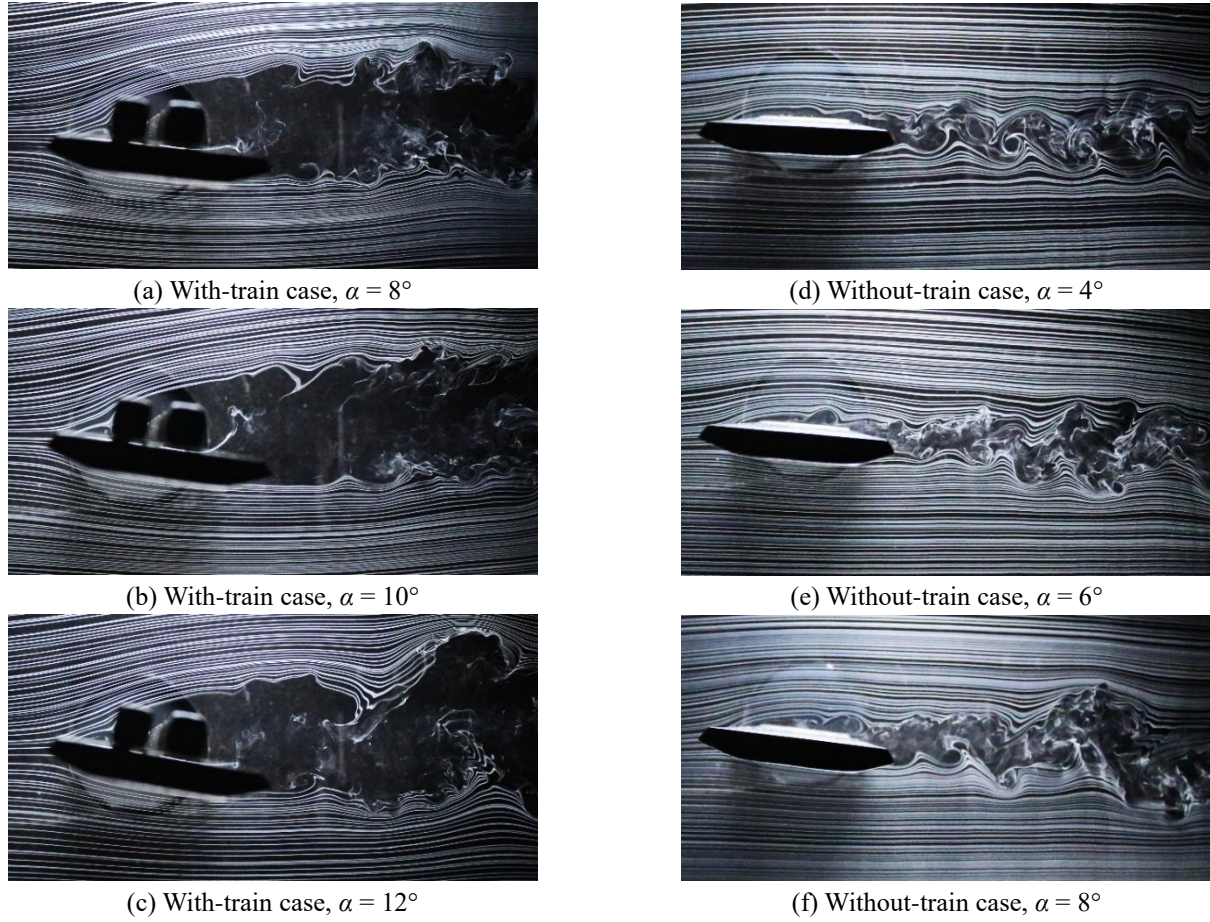


Fig. 11 Instantaneous flow structures around the streamlined bridge girder model. (a) - (c) with-train case $\alpha = 8^\circ \sim 12^\circ$, (d) - (f) without-train case $\alpha = 4^\circ \sim 8^\circ$

shedding from interior-train models, whereas the lower half is controlled by the LEVS as described in Fig. 9(a) and 9(b). In $\alpha = [-8^\circ, -6^\circ]$, the dominated flow of the upper half of the bridge-girder remains unchanged, while the above leading-edge separated flow unsteadily re-attaches on the lower half of the bridge-girder, resulting in the ILEV flow pattern, as described in Fig. 9(c) and 9(d). As pointed out by Nakamura, Ohya *et al.* (1991) and Naudascher and Wang (1993) the ILEV flow pattern causes a less organized vortex shedding for bluff bodies than other flow patterns at inflow Reynolds number larger than 2000. This explains out the foregoing disappearance of St_v observed in the range of $\alpha = [-8^\circ, -6^\circ]$. In $\alpha = [-4^\circ, 12^\circ]$, the dominated flow pattern of the upper half of the bridge-girder remains, whereas that of the lower half alters to TEVS as shown in Fig. 9(e), Figs. 10(a) - 10(e), and Fig. 11(a) - 11(c).

In comparison to the without-train case, as depicted in right columns of Figs. 9 - 11, major flow changes caused by the presence of interior-train models can be identified as follows:

For the without-train case, the dominated flow of the lower half of the bridge-girder is LEVS in $\alpha = [-16^\circ, -14^\circ]$, ILEV in $\alpha = [-12^\circ, -10^\circ]$, and TEVS in $\alpha = [-8^\circ, 8^\circ]$. But for the with-train case, the corresponding ranges of α of the above three predominated flow patterns are $[-12^\circ, -10^\circ]$, $[-8^\circ, -6^\circ]$, and $[-4^\circ, 12^\circ]$, respectively. The critical AoAs,

where flow around the lower half of the bridge-girder in the with-train case transits from LEVS to ILEV and ILEV to TEVS, are 4° smaller than those of the without-train case.

For the without-train case, the dominated flow of the lower half of the bridge-girder is TEVS in $\alpha = [-16^\circ, 4^\circ]$ and ILEV in $\alpha = [6^\circ, 8^\circ]$. In contrast, in the with-train case, this variation of flow patterns is uniformly replaced by the intensified flow separation from interior-train models. In terms of geometric scale and strength, vortices shedding from interior-train models are much larger and stronger. This intensified flow separation from interior-train models widen the near wake of the bridge-girder model.

In addition, when $\alpha = 0^\circ$, the stagnation point of oncoming flow is fixed at the upstream nose of the bridge-girder, and the global symmetrical axis of flow around the bridge-girder is located at the girder nose-tail line for the without-train case, as shown in Fig. 10(i). But for the with-train case, the stagnation point is moved to the upper surface of the bridge-girder, and the global symmetrical axis is up-shifted beyond the girder nose-tail line, as shown in Fig. 10(b). These changes indicate that the orientation of flow approaching the lower half of the bridge-girder was clockwise deflected by the presence of interior-train models. When α departs from 0° , the clockwise-deflected approaching flow of the lower half of the bridge-girder can still be detected by the upward-moved stagnation point and

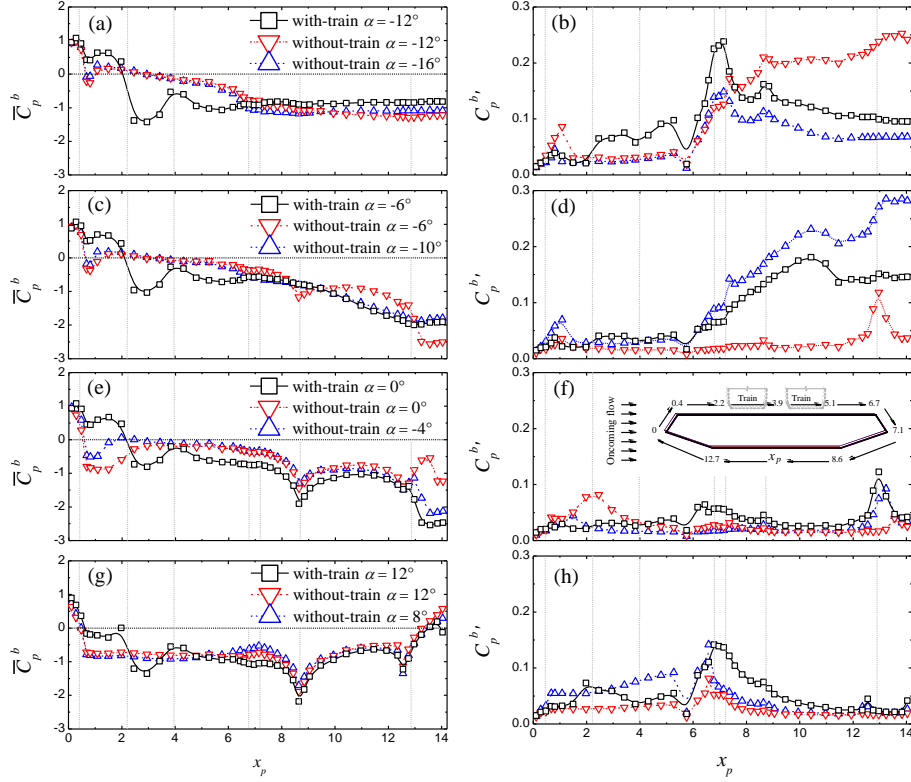


Fig. 12 Surface pressure distributions on the streamlined bridge girder model

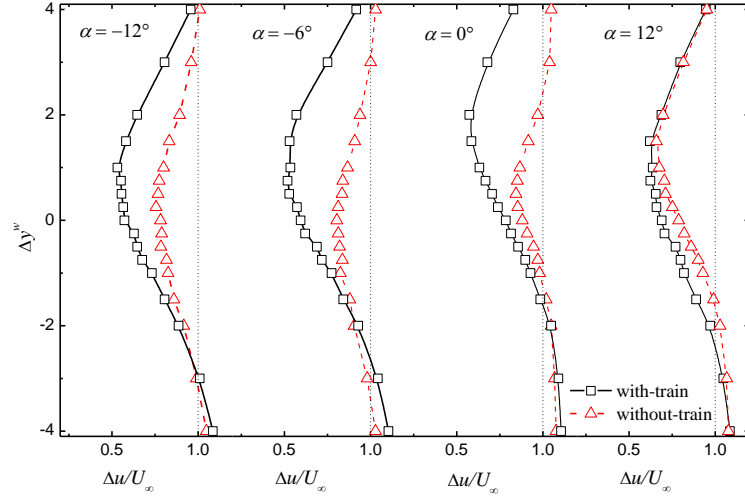


Fig. 13 Wake profiles of the streamlined bridge girder model

up-shifted global symmetrical axis. However, with an increase in $\alpha = [-12^\circ, 12^\circ]$, the upward-moved stagnation point gradually returns to the upstream nose of the bridge-girder. In other words, the aerodynamic interference of interior-trains on the bridge-girder decays as the AoA increases, which can also be quantitatively verified in section 4.3 below. Hence, the clockwise-deflected approaching flow could be the primary reason for the 4° increase in the two critical AoAs discussed above.

Based on the above discussion, the interference of two interior-train models on the lower half of the bridge-girder is manifested as an additional AoA effect, while this

interference on the upper half is depicted as an enhancement in flow separation.

4.2 Surface pressure distributions

The additional AoA effect is qualitatively detected by flow visualization in section 4.1. In order to obtain some quantitative evidence, mean and fluctuating surface pressure distributions of the lower half of the bridge-girder are discussed here. Following section 3.1, Fig. 12 only demonstrates the results tested at four selected $\alpha = -12^\circ, -6^\circ, 0^\circ$, and 12° . The surface pressure distributions of the upper

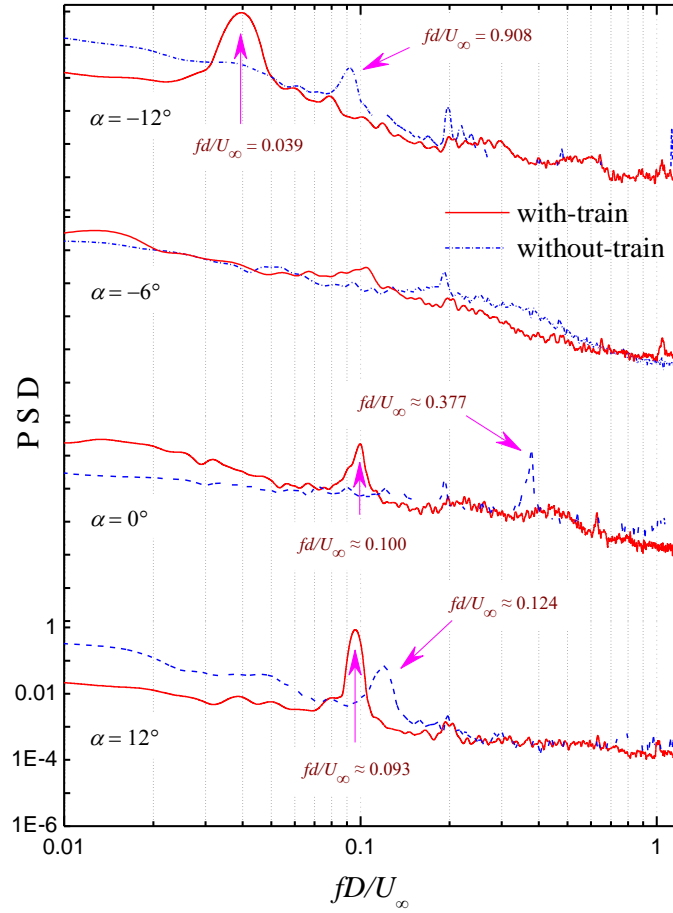


Fig. 14 PSDs of C_L^b of the streamlined bridge girder model

half of the bridge-girder are also shown here to highlight the interference caused by the presence of interior-train models.

In general, the test results of surface pressure distribution are in line with the flow visualization of the lower half of the bridge-girder. The surface pressure distributions reproduce the earlier discussion on three flow patterns reproduced by smoke-wire visualization (LEVS, ILEV, and TEVS). For $\alpha = -12^\circ$, the surface pressure around the lower half of the bridge-girder is characterized by a uniform \bar{C}_p^b of -0.85 regardless of x_p (wetted perimeter nondimensionalized by D shown in Fig. 12(f)) and a hump of $C_p^{b'}$ at the bridge-girder trailing-edge (Fig. 12(a) and (b)). They are caused by the overshooting of the leading-edge separated flow in the LEVS flow pattern as shown in Figs. 9(a) and 9(b). For $\alpha = -6^\circ$, the $C_p^{b'}$ around the lower half of the bridge-girder is significantly intensified (Fig. 12(d)), which is resulted from the thickened boundary layer observed in the ILEV flow pattern as shown in Fig. 9(c) and (d). For $\alpha = 0^\circ$ & 12° , two suction can be identified at the two lower corners of the bridge-girder model ($x_p = 8.6$ and 12.7) with $C_p^{b'}$ varying slightly. This observation indicates the leading-edge separated flow finally sheds from the bridge-girder trailing-edge, namely, the TEVS flow pattern as described in Fig. 9(e), Figs. 10(a)-10(e), and Figs. 11(a)-

11(c).

The additional AoA effect can be quantitatively recognized by the comparison of surface pressure distributions of the lower half of the bridge-girder between the with-train and without-train cases. As highlighted in Fig. 12, the surface pressure distribution in $x_p = [7.1, 14.1]$ described by the black-solid-square lines resembles that denoted by the blue-dash-up triangular ones other than the red-dash dot-down triangular ones.

4.3 Wake profiles and PSDs

The enhancement in flow separation is qualitatively identified by flow visualization in section 4.1. Similar to section 4.2, the behaviors of wake profiles and the PSDs of lift coefficients of the present streamlined bridge-girder at four selected $\alpha = -12^\circ, -6^\circ, 0^\circ$, and 12° are discussed here to provide further quantitative evidence.

Fig. 13 depicts the wake profiles of the streamlined bridge-girder model in both the with-train and without-train cases at $\alpha = -12^\circ, -6^\circ, 0^\circ$, and 12° . Obviously, the left concave in the wake profiles in the with-train case is much broader and deeper than that of the without-train case, indicating the flow separation from the bridge-girder model is enhanced by the presence of interior-train models. This observation confirms the flow visualization results in Figs. 9 - 11. Moreover, the difference in the wake profiles

decreases with an increase in α , suggesting the enhancement in flow separation decays, which is in line with the recovering stagnation point discussed in section 4.1.

Fig. 14 depicts the PSDs of lift coefficients of the streamlined bridge-girder model in both the with-train and without-train cases at $\alpha = -12^\circ$, -6° , 0° , and 12° . Consistent with the disappearance of St_v in Fig. 6, no dominant peaks can be identified at $\alpha = -6^\circ$. By comparison, the PSDs of lift coefficients in the with-train case are characterized by peaks higher than those of the without-train case, confirming the flow separation enhancement by the presence of interior-train models.

5. Conclusions

In the present paper, the aerodynamic interference effects of the two interior-trains on the aerodynamic properties of a streamlined bridge-girder are investigated experimentally by surface pressure, near wake profile, and flow visualization measurements. Major conclusions are drawn as follows:

(1) The interference on the lower half of the bridge-girder is primarily manifested by an additional angle of attack (AoA) effect. With the presence of the interior-train models, the stagnation point of the oncoming flow is upward-moved, and the global-symmetrical axis of flow around the bridge-girder is up-shifted beyond the girder nose-tail line. Equivalently, the orientation of flow approaching the bridge-girder is clockwise deflected by about 4° , in line with the increase in the stall angle of the streamlined bridge-girder and the critical AoAs where the dominant flow pattern around the bridge-girder model transits.

(2) The interference on the upper half of the bridge-girder is summarized as the enhancement in flow separation. With the presence of the interior-train models, the upper half of the bridge-girder model is always governed by the strengthened flow separation, which is responsible for the intensified fluctuating force coefficients of the bridge-girder and their span-wise correlation. Without flow reattachment on the upper half of the bridge-girder, no flow transition from trailing-edge shedding or leading-edge vortex shedding to impinging leading-edge vortices can be observed in the range of $\alpha = [0^\circ, 12^\circ]$, thus nor can an apparent stall angle be identified.

Acknowledgments

The support of the Natural Science Foundation of Hunan province (2021JJ40744), the Open Research Fund of State Key Laboratory of Mechanical Behavior and System Safety of Traffic Engineering Structures (KF2022-05), the National Natural Science Foundations of China (U1934209, 51925808), and Science and Technology Research and Development Program Project of China railway group limited (Major Special Project, 2021-Special-04-2) are gratefully acknowledged. Funding provided by the Moran Professorship in supporting this study at Notre Dame is gratefully acknowledged.

References

- Baker, C. (2014), "A review of train aerodynamics Part 1—Fundamentals", *Aeronaut. J.*, **118**(1201), 201-228. <https://doi.org/10.1017/S000192400000909X>.
- Baker, C.J. (2010), "The simulation of unsteady aerodynamic cross wind forces on trains", *J. Wind Eng. Ind. Aerod.*, **98**(2), 88-99. <https://doi.org/10.1016/j.jweia.2009.09.006>.
- Barcala, M.A. and Meseguer, J. (2007), "An experimental study of the influence of parapets on the aerodynamic loads under cross wind on a two-dimensional model of a railway vehicle on a bridge", *Proceedings of the Institution of Mechanical Engineers, Part F: Journal of Rail and Rapid Transit*, **221**(4), 487-494.
- Barcala, M.A. and Meseguer, J. (2008), "Visualization study of the influence of parapets on the flow around a train vehicle under cross winds", *WIT Transact. Built Environ.*, **103**, 797-806.
- Bocciolone, M., Cheli, F., Corradi, R., Muggiasca, S. and Tomasini, G. (2008), "Crosswind action on rail vehicles: Wind tunnel experimental analyses", *J. Wind Eng. Ind. Aerod.*, **96**(5), 584-610. <https://doi.org/10.1016/j.jweia.2008.02.030>.
- Caracoglia, L. and Jones, N.P. (2003), "Time domain vs. frequency domain characterization of aeroelastic forces for bridge deck sections", *J. Wind Eng. Ind. Aerod.*, **91**(3), 371-402. [https://doi.org/10.1016/S0167-6105\(02\)00399-9](https://doi.org/10.1016/S0167-6105(02)00399-9).
- CEN (2018), *Railway Applications. Aerodynamics. Requirements and Test Procedures for Crosswind Assessment*.
- Cheli, F., Ripamonti, F., Rocchi, D. and Tomasini, G. (2010), "Aerodynamic behaviour investigation of the new EMUV250 train to cross wind", *J. Wind Eng. Ind. Aerod.*, **98**(4-5), 189-201. <https://doi.org/10.1016/j.jweia.2009.10.015>.
- Chen, X.Z. and Kareem, A. (2002), "Advances in modeling of aerodynamic forces on bridge decks", *J. Eng. Mech.*, **128**(11), 1193-1205.
- Deniz, S. and Staubli, T. (1997), "Oscillating rectangular and octagonal profiles: Interaction of leading- and trailing-edge vortex formation", *J. Fluids Struct.*, **11**(1), 3-31. <https://doi.org/10.1006/jfls.1996.0065>.
- Diana, G., Rocchi, D., Argentini, T. and Muggiasca, S. (2010), "Aerodynamic instability of a bridge deck section model: Linear and nonlinear approach to force modeling", *J. Wind Eng. Ind. Aerod.*, **98**(6-7), 363-374. <https://doi.org/10.1016/j.jweia.2010.01.003>.
- Guissart, A., Andrianne, T., Dimitriadis, G. and Terrapon, V.E. (2019), "Numerical and experimental study of the flow around a 4:1 rectangular cylinder at moderate Reynolds number", *J. Wind Eng. Ind. Aerod.*, **189**, 289-303. <https://doi.org/10.1016/j.jweia.2019.03.026>.
- Guo, W., Wang, Y., Xia, H. and Lu, S. (2014), "Wind tunnel test on aerodynamic effect of wind barriers on train-bridge system", *Sci. China Technol. Sci.*, **58**(2), 219-225. <https://doi.org/10.1007/s11431-014-5675-1>.
- He, X.H., Li, H., Wang, H.F., Fang, D.X. and Liu, M.T. (2017), "Effects of geometrical parameters on the aerodynamic characteristics of a streamlined flat box girder", *J. Wind Eng. Ind. Aerod.*, **170**, 56-67. <https://doi.org/10.1016/j.jweia.2017.08.009>.
- Huang, R.F., Lin, B.H. and Yen, S.C. (2010), "Time-averaged topological flow patterns and their influence on vortex shedding of a square cylinder in crossflow at incidence", *J. Fluids Struct.*, **26**(3), 406-429. <https://doi.org/10.1016/j.jfluidstructs.2010.01.003>.
- Ito, Y., Shirato, H. and Matsumoto, M. (2014), "Coherence characteristics of fluctuating lift forces for rectangular shape with various fairing decks", *J. Wind Eng. Ind. Aerod.*, **135**, 34-45. <https://doi.org/10.1016/j.jweia.2014.10.003>.
- Jain, A., Jones, N.P. and Scanlan, R.H. (1996), "Coupled flutter and buffeting analysis of long-span bridges", *J. Struct. Eng.*,

- 122(7), 716-725. [https://doi.org/10.1061/\(ASCE\)0733-9445\(1996\)122:7\(716\)](https://doi.org/10.1061/(ASCE)0733-9445(1996)122:7(716)).
- Jiang, B.S., Zhou, Z.Y., Yan, K.J. and Hu, C.X. (2021), "Effect of web inclination of streamlined flat box deck on aerostatic performance of a bridge", *J. Bridge Eng.*, **26**(2). [https://doi.org/10.1061/\(ASCE\)BE.1943-5592.0001663](https://doi.org/10.1061/(ASCE)BE.1943-5592.0001663).
- Larose, G.L. and Livesey, F.M. (1997), "Performance of streamlined bridge decks in relation to the aerodynamics of a flat plate", *J. Wind Eng. Ind. Aerod.*, **69-71**, 851-860. [https://doi.org/10.1016/S0167-6105\(97\)00211-0](https://doi.org/10.1016/S0167-6105(97)00211-0).
- Larose, G.L. and Mann, J. (1998), "Gust loading on streamlined bridge decks", *J. Fluids Struct.*, **12**(5), 511-536. <https://doi.org/10.1006/jfls.1998.0161>.
- Larsen, A. and Wall, A. (2012), "Shaping of bridge box girders to avoid vortex shedding response", *J. Wind Eng. Ind. Aerod.*, **104**, 159-165. <https://doi.org/10.1016/j.jweia.2012.04.018>.
- Li, H., He, X.H., Wang, H.F. and Kareem, A. (2019), "Aerodynamics of a scale model of a high-speed train on a streamlined deck in cross winds", *J. Fluids Struct.*, **91**. <https://doi.org/10.1016/j.jfluidstructs.2019.102717>.
- Li, X.-Z., Wang, M., Xiao, J., Zou, Q.-Y. and Liu, D.-J. (2018), "Experimental study on aerodynamic characteristics of high-speed train on a truss bridge: A moving model test", *J. Wind Eng. Ind. Aerod.*, **179**, 26-38. <https://doi.org/10.1016/j.jweia.2018.05.012>.
- Li, Y., Hu, P., Xu, Y.-L., Zhang, M. and Liao, H. (2014), "Wind loads on a moving vehicle-bridge deck system by wind-tunnel model test", *Wind Struct.*, **19**(2), 145-167. <https://doi.org/10.12989/was.2014.19.2.145>.
- Li, Y., Qiang, S., Liao, H. and Xu, Y.L. (2005), "Dynamics of wind-rail vehicle-bridge systems", *J. Wind Eng. Ind. Aerod.*, **93**(6), 483-507. <https://doi.org/10.1016/j.jweia.2005.04.001>.
- Liao, H.L., Mei, H.Y., Hu, G., Wu, B. and Wang, Q. (2021), "Machine learning strategy for predicting flutter performance of streamlined box girders", *J. Wind Eng. Ind. Aerod.*, **209**, 104493. <https://doi.org/10.1016/j.jweia.2020.104493>.
- Liu, Z.W., Shen, J.S., Li, S.Q., Chen, Z.Q., Ou, Q.B. and Xin, D.B. (2021), "Experimental study on high-mode vortex-induced vibration of stay cable and its aerodynamic countermeasures", *J. Fluids Struct.*, **100**. <https://doi.org/10.1016/j.jfluidstructs.2020.103195>.
- Lystad, T.M., Fenerci, A. and Oiseth, O. (2020), "Buffeting response of long-span bridges considering uncertain turbulence parameters using the environmental contour method", *Eng. Struct.*, **213**, 110575. <https://doi.org/10.1016/j.engstruct.2020.110575>.
- Ma, C., Duan, Q., Li, Q., Chen, K. and Liao, H. (2018), "Buffeting Forces on Static Trains on a Truss Girder in Turbulent Crosswinds", *J. Bridge Eng.*, **23**(11), 04018086. [https://doi.org/10.1061/\(ASCE\)BE.1943-5592.0001305](https://doi.org/10.1061/(ASCE)BE.1943-5592.0001305).
- Ma, C.M., Wang, J.X., Li, Q.S. and Liao, H.L. (2019), "3D aerodynamic admittances of streamlined box bridge decks", *Eng. Struct.*, **179**, 321-331. <https://doi.org/10.1016/j.engstruct.2018.11.007>.
- Madaniyazi, L., Li, S., Li, S. and Guo, Y. (2020), "Candidate gene expression in response to low-level air pollution", *Environ Int.*, **140**, 105610. <https://doi.org/10.1016/j.envint.2020.105610>.
- Mannini, C., Sbragi, G. and Schewe, G. (2016), "Analysis of self-excited forces for a box-girder bridge deck through unsteady RANS simulations", *J. Fluids Struct.*, **63**, 57-76. <https://doi.org/10.1016/j.jfluidstructs.2016.02.007>.
- Montoya, M.C., Nieto, F., Alvarez, A.J., Hernandez, S., Jurado, J.A. and Sanchez, R. (2018), "Numerical simulations of the aerodynamic response of circular segments with different corner angles by means of 2D URANS. Impact of turbulence modeling approaches", *Eng. Appl. Comput. Fluid Mech.*, **12**(1), 750-779. <https://doi.org/10.1080/19942060.2018.1520741>.
- Nakamura, Y., Ohya, Y. and Tsuruta, H. (1991), "Experiments on vortex shedding from flat plates with square leading and trailing edges", *J. Fluid Mech.*, **222**, 437-447. <https://doi.org/10.1017/S0022112091001167>.
- Naudascher, E. and Wang, Y. (1993), "Flow-induced vibrations of prismatic bodies and grids of prisms", *J. Fluids Struct.*, **7**(4), 341-373. <https://doi.org/10.1006/jfls.1993.1021>.
- Ogueta-Gutiérrez, M., Franchini, S. and Alonso, G. (2014), "Effects of bird protection barriers on the aerodynamic and aeroelastic behaviour of high speed train bridges", *Eng. Struct.*, **81**, 22-34. <https://doi.org/10.1016/j.engstruct.2014.09.035>.
- Okajima, A. (1982), "Strouhal numbers of rectangular cylinders", *J. Fluid Mech.*, **123**, 379-398. <https://doi.org/10.1017/S0022112082003115>.
- Olmos, J.M. and Astiz, M.A. (2018), "Improvement of the lateral dynamic response of a high pier viaduct under turbulent wind during the high-speed train travel", *Eng. Struct.*, **165**, 368-385. <https://doi.org/10.1016/j.engstruct.2018.03.054>.
- Olmos, J.M. and Astiz, M.A. (2018), "Non-linear vehicle-bridge-wind interaction model for running safety assessment of high-speed trains over a high-pier viaduct", *J. Sound Vib.*, **419**, 63-89. <https://doi.org/10.1016/j.jsv.2017.12.038>.
- Païdoussis, M.P., Price, S.J. and De Langre, E. (2010), *Fluid-Structure Interactions: Cross-Flow-Induced Instabilities*, Cambridge University Press, New York, USA.
- Parker, R. and Welsh, M. (1983), "Effects of sound on flow separation from blunt flat plates", *Int. J. Heat Fluid Flow.*, **4**(2), 113-127. [https://doi.org/10.1016/0142-727X\(83\)90014-0](https://doi.org/10.1016/0142-727X(83)90014-0).
- Šarkić, A., Fisch, R., Höffer, R. and Bletzinger, K.-U. (2012), "Bridge flutter derivatives based on computed, validated pressure fields", *J. Wind Eng. Ind. Aerod.*, **104-106**, 141-151. "Bridge flutter derivatives based on computed, validated pressure fields."
- Sarwar, M.W., Ishihara, T., Shimada, K., Yamasaki, Y. and Ikeda, T. (2008), "Prediction of aerodynamic characteristics of a box girder bridge section using the LES turbulence model", *J. Wind Eng. Ind. Aerod.*, **96**(10-11), 1895-1911. <https://doi.org/10.1016/j.jweia.2008.02.015>.
- Suzuki, M., Tanemoto, K. and Maeda, T. (2003), "Aerodynamic characteristics of train/vehicles under cross winds", *J. Wind Eng. Ind. Aerod.*, **91**(1-2), 209-218. [https://doi.org/10.1016/S0167-6105\(02\)00346-X](https://doi.org/10.1016/S0167-6105(02)00346-X).
- Tan, B.T., Thompson, M.C. and Hourigan, K. (2003), "Sources of acoustic resonance generated by flow around a long rectangular plate in a duct", *J. Fluids Struct.*, **18**(6), 729-740. <https://doi.org/10.1016/j.jfluidstructs.2003.08.016>.
- Wang, H., Tao, T.Y., Zhou, R., Hua, X.G. and Kareem, A. (2014), "Parameter sensitivity study on flutter stability of a long-span triple-tower suspension bridge", *J. Wind Eng. Ind. Aerod.*, **128**, 12-21. <https://doi.org/10.1016/j.jweia.2014.03.004>.
- Wang, M., Li, X.-Z., Xiao, J., Zou, Q.-Y. and Sha, H.-Q. (2018), "An experimental analysis of the aerodynamic characteristics of a high-speed train on a bridge under crosswinds", *J. Wind Eng. Ind. Aerod.*, **177**, 92-100. <https://doi.org/10.1016/j.jweia.2018.03.021>.
- Wu, T. and Kareem, A. (2011), "Modeling hysteretic nonlinear behavior of bridge aerodynamics via cellular automata nested neural network", *J. Wind Eng. Ind. Aerod.*, **99**(4), 378-388. <https://doi.org/10.1016/j.jweia.2010.12.011>.
- Wu, T. and Kareem, A. (2013), "Bridge aerodynamics and aeroelasticity: A comparison of modeling schemes", *J. Fluids Struct.*, **43**, 347-370. <https://doi.org/10.1016/j.jfluidstructs.2013.09.015>.
- Xia, H., Zhang, N. and Guo, W.W. (2006), "Analysis of resonance mechanism and conditions of train-bridge system", *J. Sound Vib.*, **297**(3-5), 810-822. <https://doi.org/10.1016/j.jfluidstructs.2013.09.015>.

- Xiang, H., Li, Y. and Wang, B. (2015), "Aerodynamic interaction between static vehicles and wind barriers on railway bridges exposed to crosswinds", *Wind Struct.*, **20**(2), 237-247.
- Xiang, H., Li, Y. and Wang, B. (2015), "Aerodynamic interaction between static vehicles and wind barriers on railway bridges exposed to crosswinds", *Wind Struct.*, **20**(2), 237-247. <https://doi.org/10.12989/was.2015.20.2.237>.
- Xiang, H., Tang, P., Zhang, Y. and Li, Y. (2020), "Random dynamic analysis of vertical train-bridge systems under small probability by surrogate model and subset simulation with splitting", *Railway Eng. Sci.*, **28**(3), 305-315. <https://doi.org/10.1007/s40534-020-00219-6>.
- Xu, Y.L. and Ding, Q.S. (2006), "Interaction of railway vehicles with track in cross-winds", *J. Fluids Struct.*, **22**(3), 295-314. <https://doi.org/10.1016/j.jfluidstructs.2005.11.003>.
- Xu, Y.L., Tan, Z.X., Zhu, L.D., Zhu, Q. and Zhan, S. (2019), "Buffeting-induced stress analysis of long-span twin-box-beck bridges based on POD pressure modes", *J. Wind Eng. Ind. Aerod.*, **188**, 397-409. <https://doi.org/10.1016/j.jweia.2019.03.016>.
- Yang, W.H., Chen, W.L. and Li, H. (2020), "Suppression of vortex-induced vibration of single-box girder with various angles of attack by self-issuing jet method", *J. Fluids Struct.*, **96**. <https://doi.org/10.1016/j.jfluidstructs.2020.103017>.
- Yen, S.C. and Yang, C.W. (2011), "Flow patterns and vortex shedding behavior behind a square cylinder", *J. Wind Eng. Ind. Aerod.*, **99**(8), 868-878. <https://doi.org/10.1016/j.jweia.2011.06.006>.
- Zhou, T., Dowell, E. and Feng, S.S. (2019), "Computational investigation of wind tunnel wall effects on buffeting flow and lock-in for an airfoil at high angle of attack", *Aerosp Sci Technol.*, **95**. <https://doi.org/10.1016/j.ast.2019.105492>.
- Zhu, L.D., Meng, X.L. and Guo, Z.S. (2013), "Nonlinear mathematical model of vortex-induced vertical force on a flat closed-box bridge deck", *J. Wind Eng. Ind. Aerodyn.*, **122**, 69-82. <https://doi.org/10.1016/j.jweia.2013.07.008>.
- Zhu, Q., Xu, Y.L., Zhu, L.D. and Li, H. (2018), "Vortex-induced vibration analysis of long-span bridges with twin-box decks under non-uniformly distributed turbulent winds", *J. Wind Eng. Ind. Aerod.*, **172**, 31-41. <https://doi.org/10.1016/j.jweia.2017.11.005>.